

# Computed tomographic X-ray velocimetry for simultaneous 3D measurement of velocity and geometry in opaque vessels

S. Dubsy · R. A. Jamison · S. P. A. Higgins ·  
K. K. W. Siu · K. Hourigan · A. Fouras

Received: 12 July 2010/Revised: 30 September 2010/Accepted: 1 November 2010/Published online: 25 November 2010  
© Springer-Verlag 2010

**Abstract** Computed tomographic X-ray velocimetry has been developed for simultaneous three-dimensional measurement of flow and vessel geometry. The technique uses cross-correlation functions calculated from X-ray projection image pairs acquired at multiple viewing angles to tomographically reconstruct the flow through opaque objects with high resolution. The reconstruction is performed using an iterative, least squares approach. The simultaneous measurement of the object's structure is performed with a limited projection tomography method. An extensive parametric study using Monte Carlo simulation reveals accurate measurements with as few as 3 projection angles, and a minimum required scan angle of only 30°. When using a single/source detector system, the technique is limited to measurement of periodic or steady flow fields; however, with the use of a multiple source/detector system, instantaneous measurement will be possible. Synchrotron experiments are conducted to demonstrate the simultaneous measurement of structure and flow in a complex geometry with strong three-dimensionality. The technique will find applications in biological flow measurement, and also in engineering applications where optical access is limited, such as in mineral processing.

## 1 Introduction

Many biological flows exhibit strongly three-dimensional flow characteristics. This is especially true of the cardiovascular system. Hemodynamic properties, particularly shear, are the primary driving factor in atherosclerosis (Nesbitt 2009) and have been shown to affect the development of the heart and arterial endothelium (Hove et al. 2003). The common sites for atherosclerosis, including the carotid bifurcation and the aortic arch, are those that exhibit complex geometries and flow structures. It follows that a flow measurement technique capable of measuring blood flow fields in 3D at high resolution would be a valuable tool for research in biological fluid mechanics. Furthermore, the precise mechanical, chemical and physiological conditions in the body are difficult replicate in vitro; therefore, the ability to measure blood flow in vivo is necessary to study the effects of hemodynamic properties on atherosclerosis and cardiac development. This capability also provides a pathway for new techniques of diagnosis and treatment for cardiovascular disease.

Particle image velocimetry (PIV) is an established technique for non-invasive flow field measurement, in which a particle laden fluid is illuminated using a visible wavelength laser, and image pairs are analyzed for particle displacement using cross-correlation techniques (Adrian 2005). PIV is favored over other techniques as it provides very high resolution and accuracy. Variants exist for 3D measurement, such as  $\mu$ PIV (Hove et al. 2003; Poelma et al. 2010), tomographic PIV (Elsinga et al. 2006) and Holographic PIV (Barnhart et al. 1994). Both tomographic PIV and holographic PIV are capable of time-resolved measurement, while the scanning procedures required for 3D  $\mu$ PIV mean that only constant or periodic flows may be measured.

---

S. Dubsy (✉) · R. A. Jamison · S. P. A. Higgins ·  
K. Hourigan · A. Fouras  
Division of Biological Engineering, Monash University,  
Melbourne, VIC, Australia  
e-mail: Stephen.Dubsy@monash.edu

K. K. W. Siu  
Monash Centre for Synchrotron Science, Monash University,  
Melbourne, VIC, Australia

When particle seeding density is low, 3D particle tracking velocimetry (PTV) methods may also be used (Maas et al. 1993; Pereira et al. 2000; Troolin and Longmire 2010; Kitzhofer and Brucker 2010). The low particle seeding density required for PTV results in a reduced spatial resolution and limits these techniques to applications where strict control of seeding density is possible, which may be difficult in many biological applications.

These techniques have been applied to *in vitro* models of the cardiovascular system to characterize and study biological flows (Nesbitt et al. 2009; Vetel et al. 2009); however, the requirement of optical access has limited *in vivo* experiments to either thin-walled or transparent animal models (Hove et al. 2003; Poelma et al. 2010; Lu et al. 2008). Several groups have attempted to address this limitation by applying PIV analysis techniques to imaging modes capable of seeing through living tissue, most notably Ultrasound and X-ray imaging.

Ultrasound imaging has been combined with PIV, termed echocardiographic PIV (echo PIV) for non-invasive measurement of cardiac flows (Kheradvar et al. 2010; Kim et al. 2004), including measurement of the flow in a rat carotid artery (Niu et al. 2010). This technology has advanced to application in a clinical setting; however, those studies show severe limitations in both spatial and temporal resolution. Unfortunately, ultrasonic imaging is inherently limited by a trade-off between penetration and spatial resolution. The depth of penetration of an ultrasonic wave is inversely proportional to its wavelength; however, the spatial resolution achieved is directly proportional to its wavelength. This trade-off limits high-resolution ultrasound imaging to tissue at a depth on the order of millimeters (Niu et al. 2010) and has resulted in a spatial resolution for velocity measurements of no better than 20 mm in clinical echo PIV applications (Kheradvar et al. 2010). In fact, when comparing measurements using echo PIV with those from laser-based digital PIV *in vitro*, it was found that echo PIV was unable to resolve small-scale features of ventricular flow and also underestimated high velocity values, resulting in only a qualitative measurement of the flow-field (Kheradvar et al. 2010).

Particle tracking algorithms have been applied to images acquired using laboratory-based X-ray equipment to produce 3D flow measurement within opaque bubble columns (Seeger et al. 2001; Kertzschner et al. 2004); however, these techniques suffer from the same drawbacks as laser-based PTV methods in that the requirement for low seeding density limits the spatial resolution achieved.

PIV has been combined with synchrotron X-ray imaging to produce high-resolution measurement of flows within opaque vessels (Dubsky et al. 2010; Fouras et al. 2007; Im et al. 2007; Irvine et al. 2008, 2010; Kim and Lee 2006; Lee and Kim 2003). The coherence and brightness of

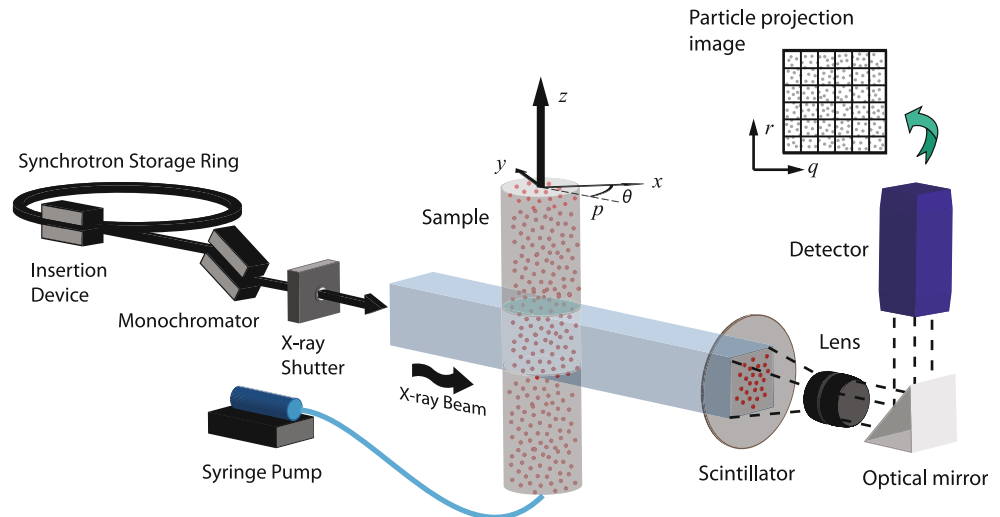
synchrotron radiation sources allow phase-contrast X-ray imaging (PCXI) to achieve ultra-fast, high-resolution imaging at higher contrast than is possible with typical absorption-based imaging (Fouras et al. 2009a). Similar in nature to in-line holographic imaging, propagation-based PCXI exploits the slight refraction of X-rays that occurs at the interfaces between materials. By allowing the X-rays to propagate some distance beyond the sample prior to detection, the transmitted and refracted rays generate interference patterns, resulting in a phase-contrast image in which weakly absorbing materials can be distinguished (Fouras et al. 2009a; Wilkins et al. 1996). Recent advances have also been made in imaging and tracer particle technology specific to X-ray PIV applications (Lee et al. 2010; Wang et al. 2008).

X-ray PIV was first applied *in vitro* using traditional two-dimensional PIV analysis techniques (Kim and Lee 2006; Lee and Kim 2003). It was then shown that since X-ray illumination produces transmission images, the image pair cross-correlation functions contain three-dimensional (3D) velocimetric information (Fouras et al. 2007). This information has been exploited in single projection techniques, using certain assumptions, to yield 3D measurement of flows within known symmetry constraints (Fouras et al. 2007; Irvine et al. 2008, 2010). The authors have recently extended these methods for general three-dimensional velocity measurement, using tomographic reconstruction based on multiple projections. This technique, computed tomographic X-ray velocimetry (CTXV) (Dubsky et al. 2010), was applied to *in vitro* blood flow, yielding high-resolution 3D velocity measurement in opaque vessels. As multiple projection images are taken, reconstruction of the vessel structure using computed tomography (CT) is also possible.

When utilizing a single source/detector imaging line, as in a standard synchrotron setup, the multiple projections are acquired by rotating the sample, limiting CTXV to time-averaged or phase-averaged measurement of constant or periodic flows. However, where all projections can be acquired simultaneously using a multiple source/detector system, instantaneous measurement may be possible.

The current paper reports new advances in the CTXV technique from the implementation described in Dubsky et al. (2010). In addition to a detailed description of the CTXV technique, new contributions include a method for increasing computational efficiency, and the addition of the simultaneous measurement of the vessel geometry. Furthermore, an extensive Monte Carlo simulation has been conducted to evaluate the effect of imaging parameters on the accuracy of velocity reconstructions. Results from *in vitro* experiments are also presented, demonstrating the application of CTXV to the 3D measurement of both the flow and geometry in an opaque vessel.

**Fig. 1** Schematic of the experimental setup for CTXV. The monochromatic X-ray beam is transmitted through the sample and is converted to visible light by the scintillator, which is imaged using a high-speed detector system to produce a projection image. Multiple projection data are gathered by rotating the sample. Cartesian co-ordinates ( $x, y, z$ ) are fixed to the sample and rotated at an angle  $\theta$  from the beam axis  $p$



## 2 Computed tomographic X-ray velocimetry

A typical imaging setup for CTXV is shown in Fig. 1. The monochromatic beam passes through the particle-seeded fluid. X-rays are slightly refracted at the interfaces between materials. The transmitted and refracted rays are allowed to propagate and interfere before being converted into visible light by the scintillator. This is then imaged using a high-speed detector and visible light optics, resulting in a phase-contrast projection image. The image results from the superposition of interference fringes generated by the particle-liquid interfaces, creating a dynamic speckle pattern that faithfully follows the particles (Fouras et al. 2007; Irvine et al. 2008, 2010).

Figure 2 illustrates the image preprocessing procedure. A raw phase-contrast image of hollow glass spheres is shown, acquired using an X-ray scintillator that is optically coupled using a fibre-optic taper to a CCD detector (Hamamatsu C9300-124S). This fibre-optic coupling replaces the lens and mirror shown in Fig. 1 and results in the honeycomb structures seen in the raw image. Horizontally oriented streaks are also apparent, which result from the crystal monochromator. Average image subtraction removes these stationary structures from the image, along with any effects due to inhomogeneous illumination, dust on the optics and the vessel walls. The average image subtraction acts as a temporal low-pass filter, and as the signal from the particles exhibits a high temporal frequency, this will remain unaffected. The phase-contrast signal from the particle interference fringes is then inverted using a phase retrieval algorithm, which is used to recover the projected thickness of the particles, preparing the images for cross-correlation analysis (Irvine et al. 2008).

Unlike visible light-based imaging systems, in which images contain focus or holographic information from which depth can be inferred (Barnhart et al. 1994; Fouras et al.

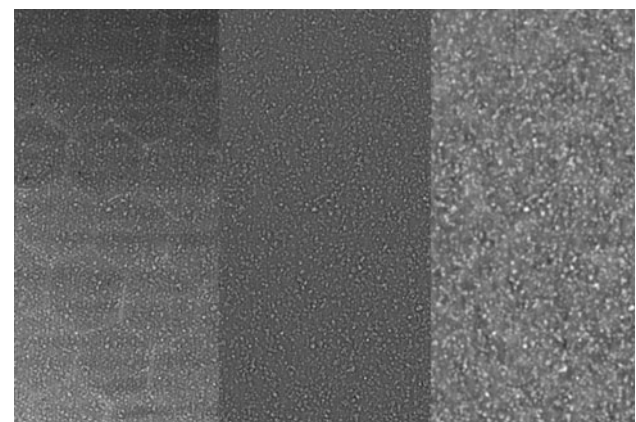


**Fig. 2** Example of image preprocessing for CTXV. Raw phase-contrast image of hollow glass spheres in glycerin (*left*). Average image subtraction removes stationary structures from the images (*middle*). Phase retrieval removes effects of interference fringes (*right*) and prepares images for cross-correlation analysis

2009b; Willert and Gharib 1992), the transmission nature of PCXI results in a two-dimensional volumetric projection image in which the entire volume is in focus, and therefore contains no information of the distribution of velocity in planes parallel to the X-ray beam propagation direction. Furthermore, from any single viewing angle, only two components of displacement can be determined. This information deficit is overcome by rotating the sample and imaging from multiple projection angles, allowing tomographic reconstruction of the velocity field within the volume. From these multiple projections, simultaneous tomographic reconstruction of the object structure is also possible.

### 2.1 Forward projection

As in traditional PIV, particle image pairs are discretized into interrogation regions, and cross-correlation is performed on

these regions. However, due to the large velocity distribution within the projected interrogation region, the cross-correlation functions will be highly distorted. The resulting projected cross-correlation statistics can be modeled as the velocity probability density function (PDF) of the flow projected onto that sub-region of the image, convolved with the particle image auto-correlation function (Fouras et al. 2007; Westerweel 2008). Therefore, if the flow field and particle image autocorrelation function are known, the cross-correlation functions that would theoretically result from the flow field can be estimated. This represents the forward projection model (Fig. 3). CTXV provides a solution for the inverse problem of reconstructing the flow field from the known cross-correlation data.

The effect of finite exposure time on the cross-correlation function of projection image pairs, as demonstrated by Fouras et al. (2007), must also be taken into account. Due to motion of the particle during the exposure, the contribution of each velocity to the cross-correlation function will be stretched along the direction of that velocity, with a magnitude that is linearly proportional to that velocity. As this effect has been well characterized, it can be easily accommodated into the forward projection model to eliminate any errors due to this phenomenon.

The spatial relationship of the reconstruction space to the image plane must be known for accurate forward projection. This can be achieved with accurate knowledge of

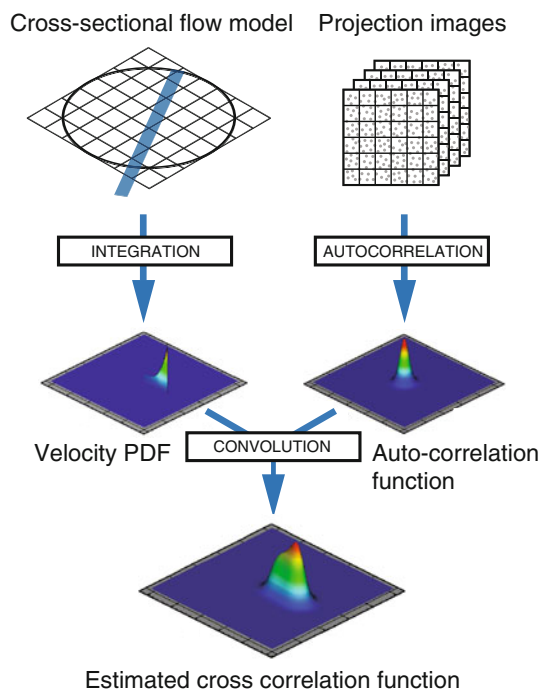


**Fig. 3** Schematic of the forward projection model. Cross-correlation functions are estimated by convolution of the velocity PDF, projected from the flow model, with the auto-correlation function calculated from the projection images

the location of the center of the rotation stage with respect to the image plane, which can be measured using several methods (Azevedo et al. 1990; Donath et al. 2006). This offset should be known to an accuracy that is better than the size of the smallest unit of tomographic reconstruction. For other methods, this unit is the 3D image voxel, but in this case, it is the much larger and more easily achieved cross-correlation interrogation window size used for the velocity reconstruction. A simple approach is to use two images of the sample acquired at projection angles separated by  $180^\circ$ . By mirroring one of these images, and cross-correlating, the offset of the center of rotation with respect to the center of the detector can be accurately calculated. Where insufficient object contrast is apparent in the images, the phase-contrast map (refer to Sect. 3) of the images may also be used for this purpose.

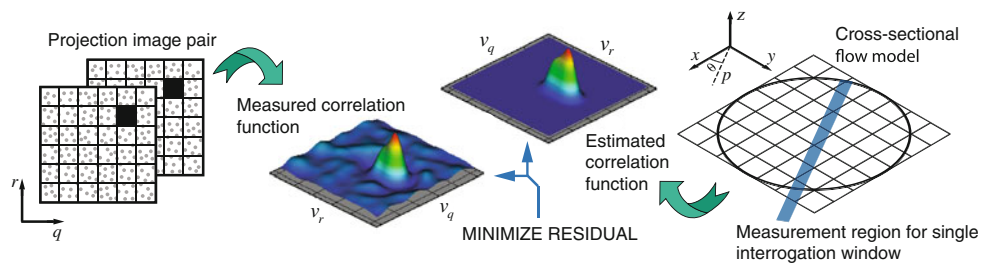
## 2.2 Solution to the inverse problem

Figure 4 demonstrates the implementation of CTXV. The velocity field is reconstructed in slices orthogonal to the axis of rotation, concurrent with the rows of interrogation regions within the projection images. A rectangular grid model represents the flow-field in the reconstruction domain. The three velocity components are defined at each node point in the model, and bi-linear interpolation is used to define the flow between node points. Higher degree interpolation schemes may be used, such as spline interpolation, at the expense of computation time and robustness.

Cross-correlation functions are estimated using the method shown in Fig. 3. The convolution is effected through a Fast Fourier Transform (FFT) implementation. A Levenberg–Marquardt algorithm is utilized to minimize the error between the cross-correlation functions estimated from the flow model and those measured from the projection image pairs, resulting in a calculated flow model that accurately represents the flow-field. As the problem is heavily over-specified, a Tikhonov-type regularization scheme is used to ensure convergence of the reconstruction, where the regularization function is equal to the sum of the difference between each node velocity value and the mean value of its neighbors.

## 2.3 One-dimensionalization of the cross-correlation

In order to reduce the required computation time and memory required for the reconstructions, a one-dimensionalization of the cross-correlation functions is performed. Projection of the cross-correlation data results in two one-dimensional representations of the function, for each of the velocity components,  $v_q$  and  $v_r$ , as illustrated in Fig. 5. The one-dimensionalization of the cross-correlation data will result in a loss of information, specifically the



**Fig. 4** CTXV reconstruction. The residual between cross-correlation functions estimated from the flow model (refer to Fig. 3) and those measured from the projection images is minimized over all

interrogation windows and all projection angles simultaneously to yield a cross-sectional flow model that accurately represents the flow-field

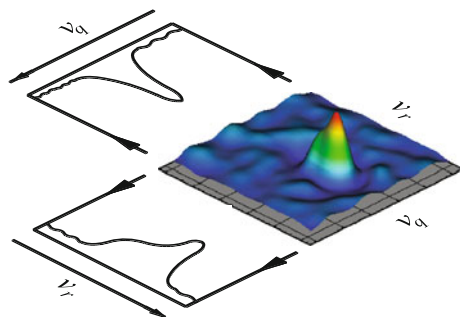


**Fig. 5** One-dimensionalization of the cross-correlation functions. Integrating across the rows and columns in the 2D cross-correlation function yields a 1D representation of the velocity PDF in the  $r$  and  $q$  directions, respectively

of each 2D correlation map of size  $a^2$  into  $2 \times 1D$  correlation maps of size  $a$  will therefore reduce the runtime by  $\frac{a^2 \log(a^2)}{2a \log(a)} = a$ . (1)

Additionally, the ability to solve for  $v_r$  and  $v_q$  separately reduces the degrees of freedom for each individual optimization and, when combined with the reduced size of the correlation data  $\mathbf{x}$ , results in significantly faster convergence of the reconstruction, and a more rapid computation of each iteration.

relationship between the two velocity components  $v_r$  and  $v_q$ ; however, this loss of information is balanced by a significant speedup in the velocity reconstruction. Additionally, by separating the two components, they can be reconstructed separately, reducing the number of parameters to be optimized for each Levenberg–Marquardt implementation.

### 3 Simultaneous structure reconstruction

The Levenberg–Marquardt implementation requires the Jacobian matrix  $\mathbf{J} = \partial \mathbf{x} / \partial \mathbf{p}$  to be calculated several times during the reconstruction, where  $\mathbf{x}$  represents the data to be fitted (the cross-correlation data), and  $\mathbf{p}$  contains the parameters in the reconstruction (i.e. the velocity values at the node points in the reconstruction domain). Due to the non-linear nature of the reconstruction,  $\mathbf{J}$  is calculated using a finite differencing scheme, requiring  $n_p$  forward projections of the reconstruction domain, where  $n_p$  is the size of  $\mathbf{p}$ .

To model the forward projection of the velocity PDF correctly, the relative particle seeding density within the reconstruction domain must be known. Assuming homogeneous seeding within the working fluid, this corresponds to knowledge of the flow geometry. We propose here a CT technique that allows the flow geometry to be reconstructed using the data obtained during the CTXV scan.

Each forward projection requires one convolution for each cross-correlation window used for the reconstruction. These convolutions represent a major component of the runtime and a substantial computational expense. For example, the results presented in Sect. 5 required  $O(10^9)$  convolutions for the reconstruction. It is well known that an FFT-based convolution requires  $O(n \log n)$  operations, where  $n$  is the size of the transformed data. The decimation

In typical CT reconstruction techniques, integrated object density in the projection direction is calculated from the X-ray transmission, which will be proportional to pixel intensity values on a digital projection image. In the case of a material of constant density, this integrated object density will be proportional to the object thickness (Kak and Slaney 2001). The contrast of the particle speckle (defined as the ratio of the standard deviation of the image intensity to the mean intensity) will increase with the square root of object thickness (Berry and Gibbs 1970), and so this statistic may also be used for tomographic reconstruction of the object’s structure. This is advantageous, as in many cases, including in vivo imaging of blood vessels, the absorption contrast alone is insufficient for tomographic reconstruction. Furthermore, the motion of the particles between images taken at different projection angles results in artifacts in the subsequent reconstructions. In comparison, the particle speckle contrast will be stationary for all viewing angles. An

example of the substantially greater signal achieved using the particle speckle contrast, when compared to the raw phase-contrast image, is shown in Sect. 5 of this paper. The particle speckle contrast is calculated for discrete sub-regions in each phase-contrast image, prior to phase retrieval. The flow geometry is reconstructed from the particle speckle contrast data using an algebraic reconstruction technique, based on the method described in Kak and Slaney (2001). The use of an algebraic technique allows for accurate reconstructions with low numbers of projections.

#### 4 Parametric study

An extensive Monte Carlo simulation was performed to elucidate the effects of the imaging parameters on CTXV reconstruction accuracy. The relevant imaging parameters for CTXV are the number of projections acquired ( $n_{proj}$ ), the number of correlation averages performed at each projection angle ( $n_{ave}$ ), the angles of projection and the particle seeding density. The minimization of  $n_{proj}$  and  $n_{ave}$  is important to reduce scan time, X-ray dose, computational expense, and in the case of a multiple source/detector configuration, equipment cost. The particle seeding density and angles of projection may be limited by the specific experiment, and so knowledge of the effects of these parameters on reconstruction accuracy is also useful.

Synthetic projection image pairs were generated using randomly positioned particles. Reconstructions were performed with varying  $n_{proj}$  and  $n_{ave}$ , and the total scan angle. Each data point in the results represents the statistics of 128 individual reconstructions. The root mean square (RMS) error is calculated as,

$$\sqrt{\frac{\sum_{x,y,z} [\varepsilon_x^2 + \varepsilon_y^2 + \varepsilon_z^2]}{3N}}, \quad (2)$$

where  $\varepsilon_x$ ,  $\varepsilon_y$ , and  $\varepsilon_z$  are the absolute errors in  $v_x$ ,  $v_y$ , and  $v_z$ , respectively, and  $N$  is the total number of vectors used in

the ensemble. Reconstructions that exhibit an RMS error of less than 1 pixel (px) are deemed acceptable. Two flow cases were studied, an axisymmetric flow and an asymmetric flow (Fig. 6). The axisymmetric flow is made up of a parabolic  $v_z$  profile with a diverging  $v_x$  and  $v_y$  flow, with a maximum displacement between frames of 10 px. The asymmetric case exhibits a reversing  $v_z$  profile with mono-directional cross-flow, with a maximum displacement between frames of 20 px.

Figure 7 shows the combined RMS error, plotted against both  $n_{ave}$  and effective seeding density. Here, effective seeding density is defined as the seeding density for a single image multiplied by  $n_{ave}$ . Correlation averaging will have an equivalent effect on the quality of the cross-correlation statistics as an increase in effective seeding density (Westerweel 2004). This metric is intended as an indication of the number of particles used in the correlation statistics and does not account for image noise or errors due to false correlations. In general, an increase in  $n_{ave}$  will improve the quality of the correlation map to a higher degree than an equivalent increase in the absolute seeding density; however, both will result in higher quality correlation maps. Projections were equally spaced over  $180^\circ$ .

As expected, an increase in  $n_{ave}$  gives a reduction in error. Importantly, acceptable results are obtained with as few as 3 projections. The RMS error continues to reduce as effective seeding density increases past 1 particle per pixel (ppp). Due to the volumetric nature of PCXI, these high seeding densities can be easily obtained in X-ray PIV experiments. The reconstructions of the asymmetric flow case exhibit greater errors. This is most likely due to a wider distribution of velocities present in the flow-field, causing a more elongated correlation function, and thus a lower signal to noise ratio.

The average error for all reconstructions was found to be below 1% of the maximum velocity, indicating that the errors found in the simulation are predominantly random errors. A slight bias error acts to underestimate the

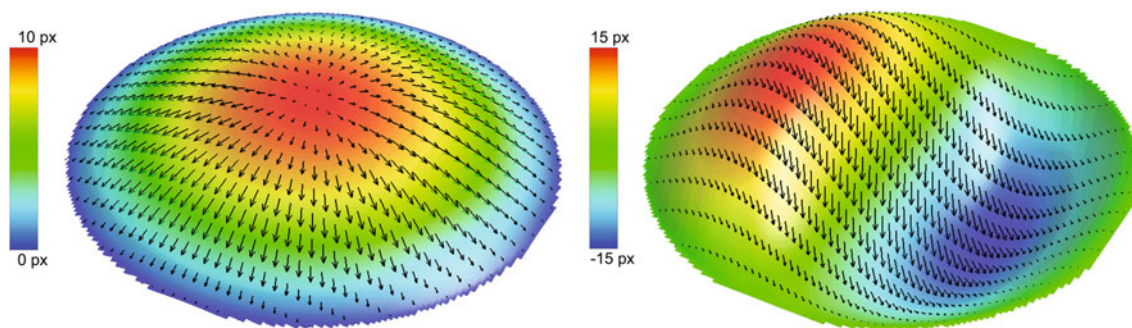
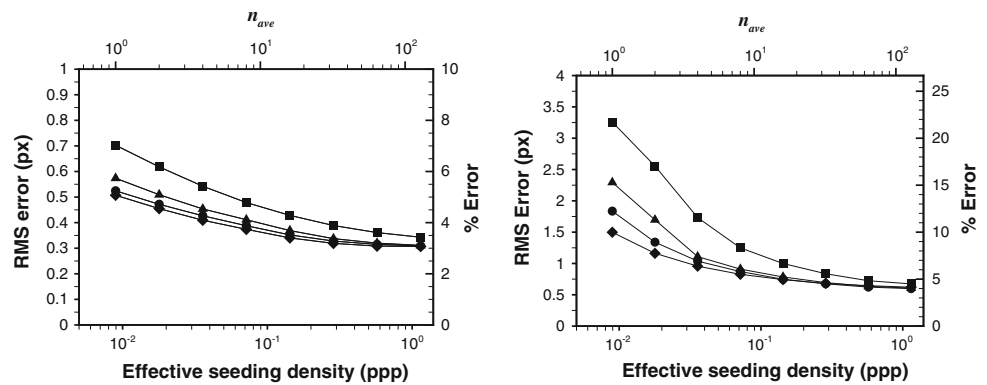


**Fig. 6** Flow-fields used for synthetic image generation: Axisymmetric flow-field (*left*), with parabolic  $v_z$  profile and diverging  $v_x$  and  $v_y$  velocities, and asymmetric flow-field (*right*), with reversing  $v_z$  profile

and mono-directional cross-flow. Surface and colors indicate  $v_z$  component, and vectors show the  $v_x$  and  $v_y$  components

**Fig. 7** RMS Error vs.  $n_{ave}$  for axisymmetric case (left) and asymmetric case (right), for  $n_{proj} = 3$  (filled square),  $n_{proj} = 6$  (filled triangle),  $n_{proj} = 9$  (filled circle), and  $n_{proj} = 18$  (filled diamond). Results show acceptable accuracy using as few as 3 projections, provided the effective seeding density is sufficiently high



velocity. This is most likely caused by the linear interpolation used in the reconstruction. This may be resolved by using higher-order interpolation schemes, at the cost of computational efficiency.

Figure 8 shows the same data plotted against effective dose (defined as the number of image pairs acquired over the total scan, that is,  $n_{proj} \times n_{ave}$ ), expressed as a percentage of the maximum displacement. The data converge onto a single curve, indicating that the reconstruction accuracy is related to the effective dose and that this relationship is largely independent of the number of projections. This is an important distinction from typical CT reconstruction, in which the accuracy of the reconstructions is strongly related to the number of projections. This difference is explained by considering the amount of information gathered from each projection. While conventional CT uses projected line-integrals, the use of the cross-correlation allows the projected velocity PDF to be extracted from the projections, and hence, far more information is available for the reconstruction. This result is significant and guides the experimentalist in the choice of

imaging parameters. For example, if fewer projections are available, one must increase image quality, number of correlation averages, or seeding density, or conversely, the addition of more projections may be used to overcome poor image quality.

Figure 9 shows the effect of the total scan angle on the RMS error for 3 and 6 projections. To eliminate any effects of directionality in the flow-field, this study was performed only on the axisymmetric flow case; however, the trends will be qualitatively valid for general flow fields. An optimal total scan angle of  $120^\circ$  was found for 3 projections (i.e. 2 increments of  $60^\circ$  each) and  $150^\circ$  for 6 projections (i.e. 5 increments of  $30^\circ$  each), representing equal spacing over  $180^\circ$  (exclusive). This is not surprising, as projections spaced  $180^\circ$  apart are equivalent, and therefore, the inclusion of a  $180^\circ$  projection is redundant. It should also be noted that the minimum total scan angle for acceptable results to be obtained is  $30^\circ$ , which may be important where access to the sample is limited.

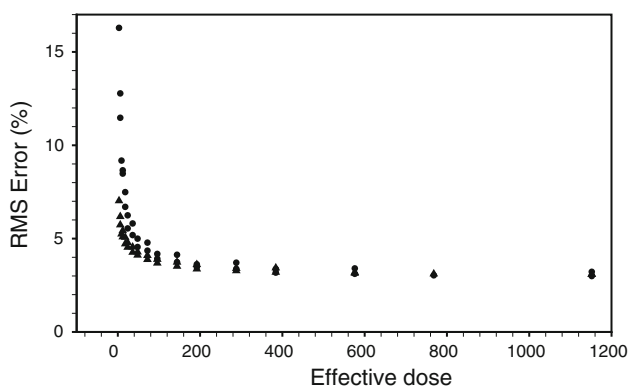


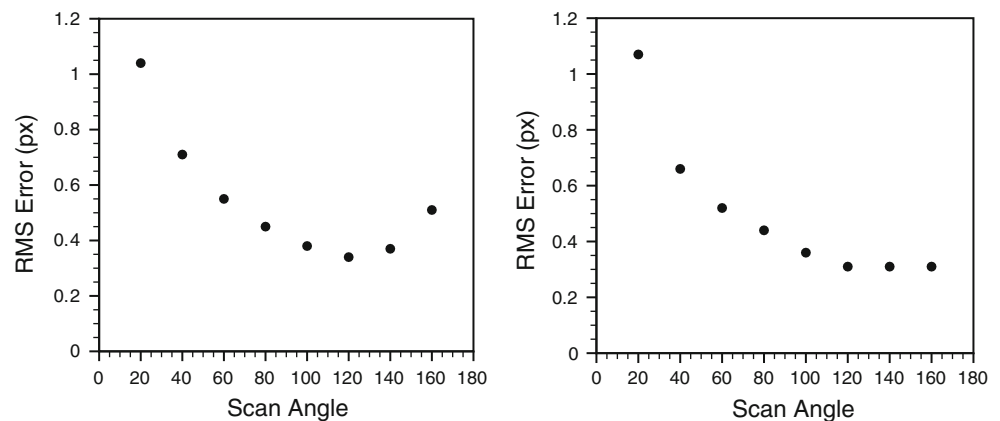
**Fig. 8** RMS error versus effective dose ( $n_{proj} \times n_{ave}$ ) for axisymmetric (filled triangle) and asymmetric (filled circle) flow-fields. Data collapse onto a single curve for all numbers of projections, indicating that the error is proportional to effective dose, and independent of the number of projections

## 5 Experimental application

Experiments were performed to demonstrate the application of CTXV to the simultaneous measurement of structure and velocity. Experiments were conducted at the SPring-8 Synchrotron, Hyogo Japan, on the medical imaging beamline BL20B2.

The sample used was an opaque plastic model, with a complex three-dimensional geometry, manufactured using Objet<sup>TM</sup> rapid prototyping technology. The test section consisted of a solid cylinder of 14 mm diameter, with a hollow section allowing internal flow of the working fluid (Fig. 10). The geometry of the hollow section was constructed as the union of a cone and a helically swept circle, resulting in corkscrew geometry with a decreasing cross-sectional area. The geometry was chosen to exhibit a strongly three-dimensional flow. The working fluid,

**Fig. 9** Total scan angle versus RMS error for the axisymmetric test case for  $n_{proj} = 3$  (left), and  $n_{proj} = 6$  (right),  $n_{ave} = 128$ . Results indicate that an equal spacing over  $180^\circ$  is optimal ( $120^\circ$  for 3 projections, and  $150^\circ$  for 6 projections)



glycerin seeded with  $35\ \mu\text{m}$  (nominal) solid glass spheres (Spheriglass A, Potters Inc.), was pumped through the model at  $0.1\ \text{ml/min}$  using a syringe pump (Harvard Apparatus, PHD 22/2000). The propagation distance, defined as the distance from the front face of the object to the scintillator, was optimized for maximum signal to noise ratio of the glycerin/glass mixture at  $6\text{m}$ .

The imaging setup used for the experiment is illustrated in Fig. 1. The BL20B2 beamline uses a bending magnet insertion device. An X-ray energy of  $25\ \text{keV}$  was selected using an Si-111 monochromator. A fast X-ray shutter was used to minimize sample dose, and also to protect the P43 scintillator from the high flux X-ray beam. An EM-CCD detector (Hamamatsu C9100-02) was used for its sensitivity and low-noise characteristics. The optics used resulted in an effective pixel size of  $9.5 \times 9.5\ \mu\text{m}$ , allowing a field of view of  $9.5\ \text{mm} \times 9.5\ \text{mm}$ . Images were acquired at 19 angles, evenly spaced over  $180^\circ$  (inclusive). The  $180^\circ$  projection was included to allow the calculation of the center of rotation of the sample; however, this may be excluded in place of a simple calibration/alignment process. The detector acquired images at 2.85 frames per second with an exposure time of  $300\ \text{ms}$ .

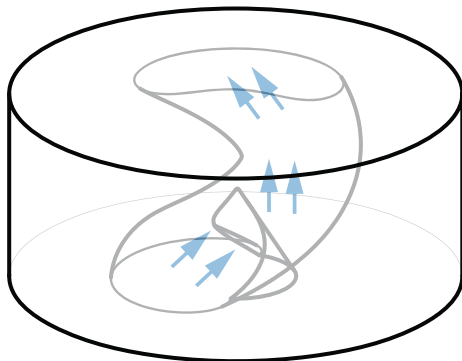


**Fig. 10** Schematic of the test section of the experimental model, consisting of a solid cylinder with a hollow section allowing internal flow of the working fluid. Arrows indicate flow direction

The flow geometry was reconstructed using the method described in Sect. 3. Figure 11 clearly demonstrates the substantially higher signal achieved using the particle speckle contrast data when compared to the raw phase-contrast image. The speckle contrast map was generated using  $16 \times 16\ \text{px}^2$  sub-regions with 50% overlap. Figure 12 shows the computer-aided design (CAD) model used for the manufacture of the hollow section of the flow model and the tomographically reconstructed geometry, segmented using a gradient-based edge detection method.

For the velocity reconstruction, cross-correlation functions were calculated using  $64 \times 64\ \text{px}^2$  interrogation windows with 75% overlap. Correlation averaging was used with an ensemble of 99 image pairs taken at each projection angle to produce the averaged correlation data. The 69 axial slices were individually reconstructed using a rectangular grid, with a spacing of approximately  $350\ \mu\text{m}$ , interpolated onto the structural reconstruction domain (Fig. 13). This results in the use of a velocity value for each planar voxel within the object reconstruction being utilized for the cross-correlation estimation, and hence a vector spacing of  $8\ \text{px}$ .

The resulting structure and velocity fields are shown in Fig. 14. As expected, the flow follows the helical geometry, increasing in speed as the vessel constricts through the cone section. The results illustrate the ability of the technique to measure complex 3D flows, even with few projections.

To demonstrate the statistical convergence in the correlation ensemble, the number of image pairs used to generate the correlation data at each projection ( $n_{ave}$ ) was varied from 1 to 75. The RMS error between these reconstructions and those using the full set of 99 image pairs was calculated using Eq. 1 and expressed as a percentage of the maximum velocity ( $|v|_{max} = 11.51\ \text{px}$ ) (Fig. 15). The trend shown in the Monte-Carlo simulation is confirmed by the results (Figs. 7 & 8). The results show only a small decrease in the RMS error of the

**Fig. 11** Phase-contrast image (*left*) of sample and corresponding particle speckle contrast map (*right*), demonstrating the substantially greater signal achieved by using the speckle contrast data. Both figures show the average data from 100 images

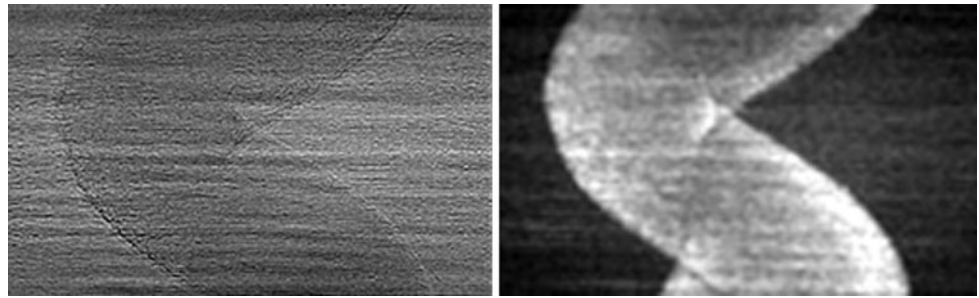


**Fig. 12** Computer-aided design model used for the hollow section of the sample (*red*), and CT reconstruction based on the particle speckle contrast (*blue*). The geometry consists of the union of a cone and a helically swept circle

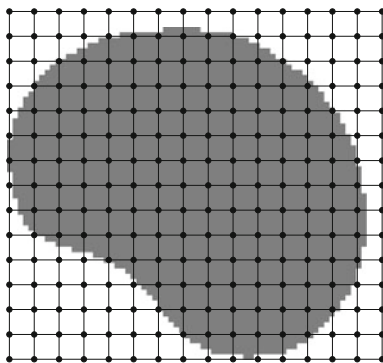
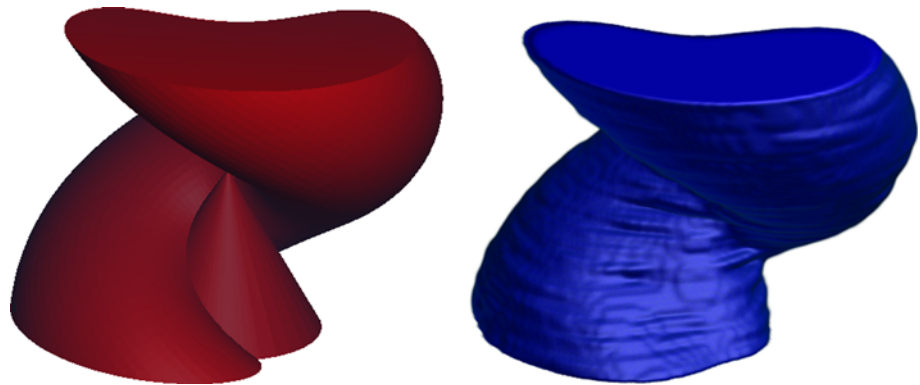


**Fig. 13** Illustration of the velocity reconstruction domain for a single axial slice. The velocity is reconstructed on a rectangular grid, interpolated onto the object geometry shown in *grey*

reconstructions for an increase in  $n_{ave}$  from 50 to 75, when compared with the reconstructions using 99 averages, indicating an adequate number of image pairs in the analysis.

To further validate the accuracy of the reconstructions, the divergence of the vector field was calculated. As the flow can be considered incompressible, the principle of continuity dictates that the flow will exhibit zero divergence, that is

$$\nabla \cdot \mathbf{v} = \frac{\partial v_x}{\partial x} + \frac{\partial v_y}{\partial y} + \frac{\partial v_z}{\partial z} = 0. \quad (3)$$

The partial derivatives in Eq. 3 were calculated using the method described in Fouras and Soria (1998). By

multiplying  $\nabla \cdot \mathbf{v}$  by the vector pixel spacing (8 px), the divergence can be calculated in terms of pixel velocity. The divergence in the reconstruction exhibits an approximately random spatial distribution, with slightly more divergence present in reconstruction planes that contain higher velocities. This is not surprising, as the reconstruction errors in these regions are expected to be larger, due to the reduction in the SNR of the correlation functions resulting from the wider velocity distribution, as shown in the parametric study (Sect. 4). Figure 16 shows a histogram of the divergence of the reconstructed vector field, expressed as a percentage of the maximum velocity ( $|\mathbf{v}|_{max} = 11.51 \text{ px}$ ). The reconstruction has an average divergence of 0.017% (0.002 px) with 99% of voxels exhibiting an absolute divergence less than 3.48% (0.40 px). These results show that the reconstructed 3D vector field is consistent with the principle of continuity, indicating a high level of accuracy.

## 6 Summary and conclusions

We have developed and applied the CTXV technique for simultaneous velocity and structure measurement for flow in opaque vessels. Through Monte Carlo simulation, it was demonstrated that accurate reconstructions can be obtained with as few as 3 projections and as little as  $30^\circ$  total scan angle, provided sufficient image quality is achieved. It was shown that accuracy is determined by the effective dose

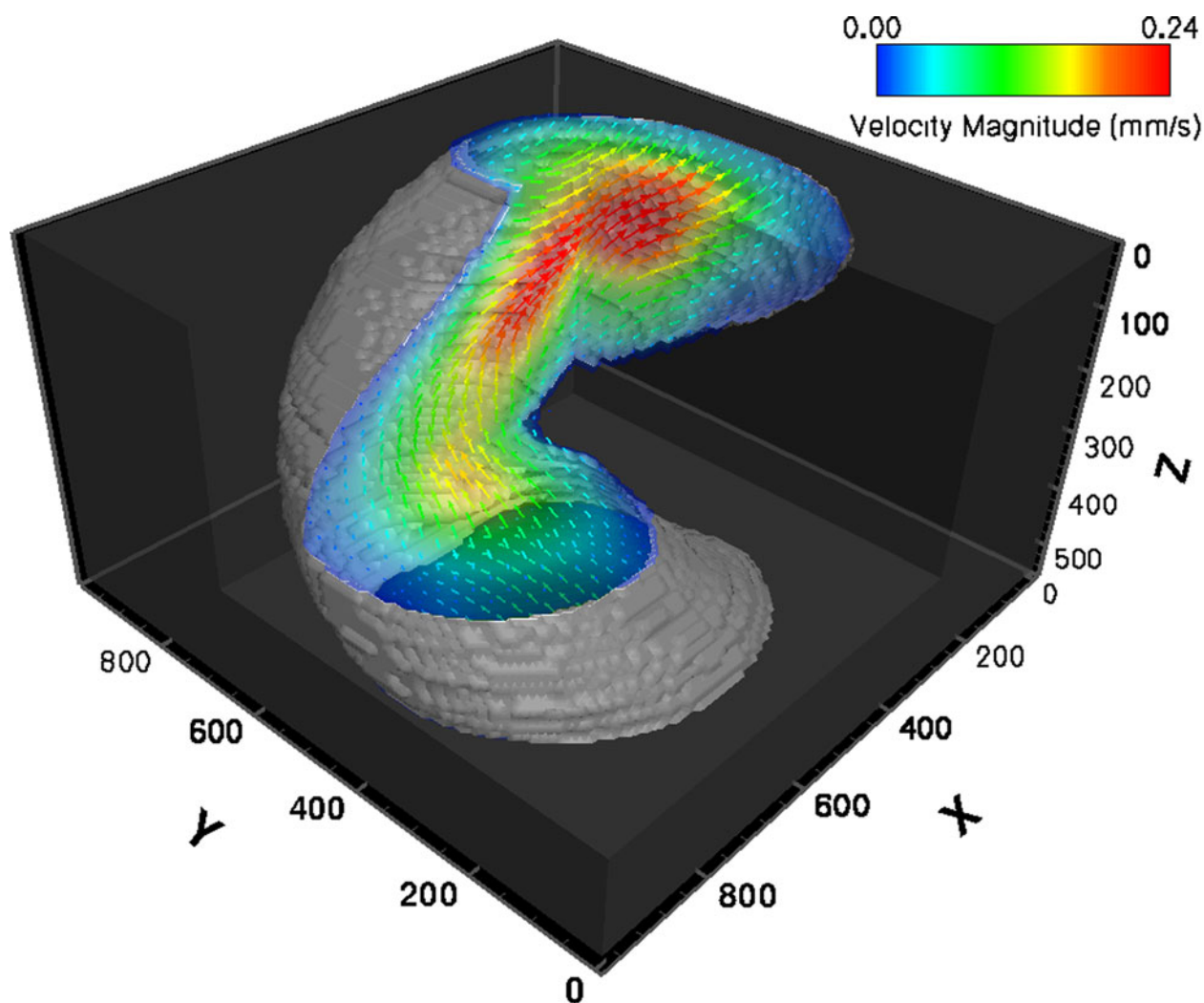


**Fig. 14** CTXV reconstruction of flow through helical geometry. A section of the result has been rendered as transparent for visualization of the flow. Colors represent velocity magnitude. For clarity, vector

resolution is reduced by  $4 \times$  in  $x$ ,  $y$ , and  $z$ . The results illustrate the ability of CTXV to simultaneously measure the 3D structure and velocity of flow through complex geometries

( $n_{proj} \times n_{ave}$ ) and that this relationship is largely independent of the number of projections acquired. Accurate results were demonstrated in a complex flow with strong three-dimensionality in both structure and velocity.

The use of a single source/detector configuration limits the application of CTXV to time-averaged or phase-averaged measurement of constant or periodic flows. However, the low numbers of projections required for accurate velocity reconstruction open the possibility of instantaneous measurement using a multiple source/detector setup, which could be based on laboratory phase-contrast X-ray sources. Furthermore, as many biological flows, such as blood flow, are periodic, phase-averaged measurements are adequate to characterize the fluid mechanics in these systems.

With little adaptation, the technique may also be used in conjunction with imaging modes other than PCXI such as visible laser light or infrared imaging. This may be useful for applications with limited access, or cases where specialized or expensive cameras are needed, prohibiting the use of multi-camera set-ups required by other laser-based techniques.

Recent developments in ultrafast synchrotron imaging (Wang et al. 2008) and X-ray PIV tracer particles (Lee et al. 2010) will result in the capability to image flows at physiological rates, allowing application of this technique to in vivo measurement of blood flow. Engineering applications may also be found where optical access is limited, for example in the mineral processing or automotive industries.

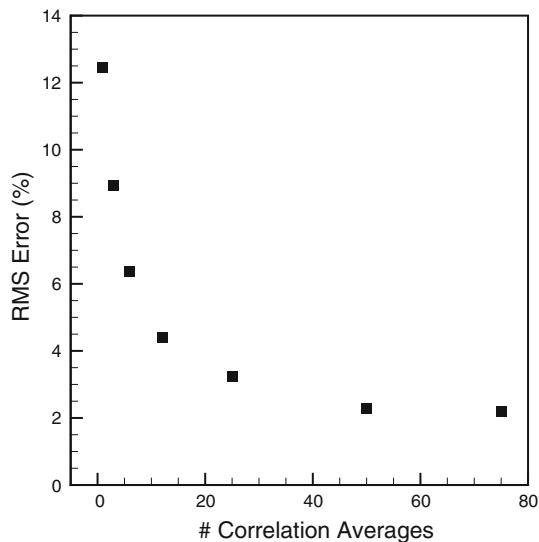


**Fig. 15** RMS error versus  $n_{ave}$  for experimental data. RMS error is expressed as a percentage of the maximum velocity ( $|v|_{max} = 11.51$  px), and calculated by comparison to reconstructions using  $n_{ave} = 99$

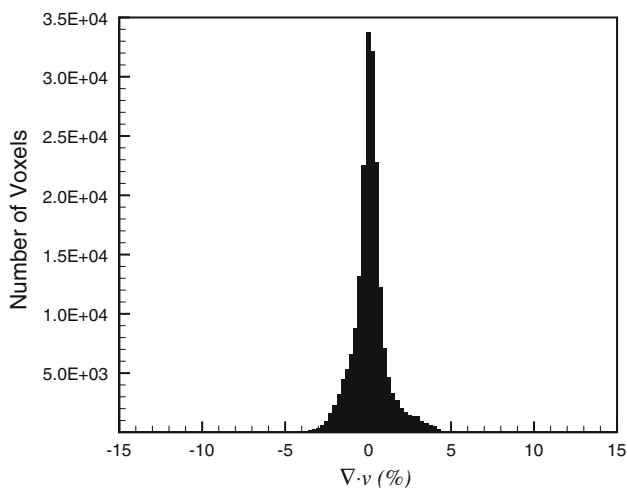


**Fig. 16** Histogram of the divergence of the reconstructed vector field, expressed as a percentage of the maximum velocity ( $|v|_{max} = 11.51$  px). The reconstruction has an average divergence of 0.017% (0.002 px) with 99% of voxels exhibiting an absolute divergence less than 3.48% (0.40 px)

**Acknowledgments** The authors gratefully acknowledge the support of the Japan Synchrotron Radiation Research Institute (JASRI) under Proposal Nos. 2009A0022 and 2009A1882. The authors would like to thank Prof. Naoto Yagi and Dr. Kentaro Uesugi of SPring-8/JASRI for their assistance with the experiments. Support from the Australian Research Council (Grant Nos. DP0877327, DP0987643) is also gratefully acknowledged.

## References

Adrian RJ (2005) Twenty years of particle image velocimetry. *Exp Fluids* 39:159–169

- Azevedo SG, Schneberk DJ, Fitch JP, Martz HE (1990) Calculation of the rotational centers in computed tomography sinograms. *IEEE Trans Nucl Sci* 37:1525–1540
- Barnhart DH, Adrian RJ, Papen GC (1994) Phase-conjugate holographic system for high-resolution particle-image velocimetry. *Appl Opt* 33:7159–7170
- Berry MV, Gibbs DF (1970) Interpretation of optical projections. *Proc R Soc Lond Ser A* 314:143
- Donath T, Beckmann F, Schreyer A (2006) Automated determination of the center of rotation in tomography data. *J Opt Soc Am* 23:1048–1053
- Dubsky S, Jamison RA, Irvine SC, Siu KKW, Hourigan K, Fouras A (2010) Computed tomographic x-ray velocimetry. *Appl Phys Lett* 96:023702
- Elsinga GE, Scarano F, Wieneke B, van Oudheusden BW (2006) Tomographic particle image velocimetry. *Exp Fluids* 41:933–947
- Fouras A, Soria J (1998) Accuracy of out-of-plane vorticity measurements derived from in-plane velocity field data. *Exp Fluids* 25:409–430
- Fouras A, Dusting J, Lewis R, Hourigan K (2007) Three-dimensional synchrotron x-ray particle image velocimetry. *J Appl Phys* 102:064916
- Fouras A, Kitchen MJ, Dubsky S, Lewis RA, Hooper SB, Hourigan K (2009) The past, present, and future of x-ray technology for in vivo imaging of function and form. *J Appl Phys* 105:102009
- Fouras A, Lo Jacono D, Nguyen CV, Hourigan K (2009) Volumetric correlation PIV: a new technique for 3D velocity vector field measurement. *Exp Fluids* 47:569–577
- Hove JR, Koster RW, Forouhar AS, Acevedo-Bolton G, Fraser SE, Gharib M (2003) Intracardiac fluid forces are an essential epigenetic factor for embryonic cardiogenesis. *Nature* 421:172–177
- Im KS, Fezzaa K, Wang YJ, Liu X, Wang J, Lai MC (2007) Particle tracking velocimetry using fast x-ray phase-contrast imaging. *Appl Phys Lett* 90:091919
- Irvine SC, Paganin DM, Dubsky S, Lewis RA, Fouras A (2008) Phase retrieval for improved three-dimensional velocimetry of dynamic x-ray blood speckle. *Appl Phys Lett* 93(15):153901
- Irvine SC, Paganin DM, Jamison A, Dubsky S, Fouras A (2010) Vector tomographic X-ray phase contrast velocimetry utilizing dynamic blood speckle. *Opt Express* 18:2368–2379
- Kak AC, Slaney M (2001) Principles of computerized tomographic imaging. Society of Industrial and Applied Mathematics, Philadelphia
- Kertzscher U, Seeger A, Affeld K, Goubergrits L, Wellenhofer E (2004) X-ray based particle tracking velocimetry—a measurement technique for multi-phase flows and flows without optical access. *Flow Meas Instrum* 36:455–462
- Kheradvar A, Houle H, Pedrizzetti G, Tonti G, Belcik T, Ashraf M, Lindner JR, Gharib M, Sahn D (2010) Echocardiographic particle image velocimetry: a novel technique for quantification of left ventricular blood vorticity pattern. *J Am Soc Echocardiogr* 23:86–94
- Kim GB, Lee SJ (2006) X-ray PIV measurements of blood flows without tracer particles. *Exp Fluids* 41:195–200
- Kim HB, Hertzberg JR, Shandas R (2004) Development and validation of echo PIV. *Exp Fluids* 36:455–462
- Kitzhofer J, Brucker C (2010) Tomographic particle tracking velocimetry using telecentric imaging. *Exp Fluids*
- Lee SJ, Kim GB (2003) X-ray particle image velocimetry for measuring quantitative flow information inside opaque objects. *J Appl Phys* 94:3620–3623
- Lee SJ, Jung SY, Ahn S (2010) Flow tracing microparticle sensors designed for enhanced X-ray contrast. *Biosens Bioelectron* 25:1571–1578

- Lu J, Pereira F, Fraser SE, Gharib M (2008) Three-dimensional real-time imaging of cardiac cell motions in living embryos. *J Biomed Opt* 13(1):014006
- Maas HG, Gruen A, Papantoniou D (1993) Particle tracking velocimetry in three-dimensional flows. *Exp Fluids* 15:133–146
- Nesbitt WS, Westein E, Tovar-Lopez FJ, Tolouei E, Mitchell A, Fu J, Carberry J, Fouras A, Jackson SP (2009) A shear gradient-dependent platelet aggregation mechanism drives thrombus formation. *Nat Med* 15:665–U146
- Niu L, Qian M, Wan K, Yu WT, Jin QF, Ling T, Gao S, Zheng HR (2010) Ultrasonic particle image velocimetry for improved flow gradient imaging: algorithms, methodology and validation. *Phys Med Biol* 55:2103–2120
- Poelma C, Vander Heiden K, Hierck BP, Poelmann RE, Westerweel J (2010) Measurements of the wall shear stress distribution in the outflow tract of an embryonic chicken heart. *J R Soc Interface* 7:91–103
- Pereira F, Gharib M, Dabiri D, Modarress D (2000) Defocusing digital particle image velocimetry: a 3-component 3-dimensional DPIV measurement technique. *Exp Fluids* 29(7):S78–S84
- Seeger A, Affeld K, Goubergrits L, Kertzsch U, Wellnhofer E (2001) X-ray-based assessment of the three-dimensional velocity of the liquid phase in a bubble column. *Exp Fluids* 31:193–201
- Troolin DR, Longmire EK (2010) Volumetric velocity measurements of vortex rings from inclined exits. *Exp Fluids* 48:409–420
- Vetel J, Garon A, Pelletier D (2009) Lagrangian coherent structures in the human carotid artery bifurcation. *Exp Fluids* 46:1067–1079
- Wang YJ, Liu X, Im KS, Lee WK, Wang J, Fezzaa K, Hung DLS, Winkelman JR (2008) Ultrafast X-ray study of dense-liquid-jet flow dynamics using structure-tracking velocimetry. *Nat Phys* 4:305–309
- Westerweel J (2008) On velocity gradients in PIV interrogation. *Exp Fluids* 44:831–842
- Westerweel J, Geelhoed PF, Lindken R (2004) Single-pixel resolution ensemble correlation for micro-PIV applications. *Exp Fluids* 37:375–384
- Wilkins SW, Gureyev TE, Gao D, Pogany A, Stevenson AW (1996) Phase-contrast imaging using polychromatic hard X-rays. *Nature* 384:335–338
- Willert CE, Gharib M (1992) 3-Dimensional particle imaging with a single camera. *Exp Fluids* 12:353–358